On the influence of the local maxima of total pressure on the current sheet stability to the kink-like (flapping) mode

D. B. Korovinskiy,[1, a)] N. V. Erkaev,[2, 3] V. S. Semenov,[4] I. B. Ivanov,[5] S. A. Kiehas,[1] and I. I. Ryzhkov[2]

[1)] *Space Research Institute, Austrian Academy of Sciences, 8042, Schmiedlstrasse 6, Graz, Austria*

[2)] *Institute of Computational Modelling, FRC "Krasnoyarsk Science Center" SBRAS, 660036, Krasnoyarsk, Russia.*

[3)] *Siberian Federal University, 660041, Krasnoyarsk, Russia.*

[4)] *Saint Petersburg State University, 198504, Ulyanovskaya 1, Petrodvoretz, Russia*

[5)] *Theoretical Physics Division, Petersburg Nuclear Physics Institute, 188300, Gatchina, Russia.*

(Dated: 11 January 2018)

Stability of the Fadeev-like current sheet with respect to transversally propagating kink-like perturbations (flapping mode) is considered in terms of two-dimensional linear MHD numerical simulations. It is found that the current sheet is stable when the total pressure minimum is located in the sheet center, and unstable when the maximum value is reached there. It is shown that an unstable spot of any size enforces the whole sheet to be unstable, though the increment of instability decreases with the reduction of the unstable domain. In unstable sheets the dispersion curve of instability shows a good match with the double-gradient (DG) model prediction. Here, the typical growth rate (short-wavelength limit) is close to the DG estimate averaged over the unstable region. In stable configurations the typical frequency matches the maximum DG estimate. The dispersion curve of oscillations demonstrates a local maximum at wavelength ~ 0.7 sheet half-width, which is a new feature absent in simplified analytical solution.

PACS numbers: 47.35.Tv, 52.30.-q, 52.35.-g, 94.30.cl, 94.30.cq, 94.30.cs
Keywords: flapping oscillations, double-gradient model, magnetotail dynamics, MHD plasma stability

[a)]Electronic mail: daniil.korovinskiy@oeaw.ac.at

I. INTRODUCTION

In the present paper we focus on the magnetohydrodynamic (MHD) stability of magnetotail-like current sheets to kink-like perturbations propagating in the dawn-dusk direction. Perturbations of such kind are known as flapping oscillations, registered in numerous *in-situ* observations at the Earth[1–8], Venus[9], Jupiter and Saturn[10,11]. Particularly, in the Earth midtail ($\sim 10-30\,Re$, where Re is the Earth radius) long-wavelength ($\lambda \sim$ several Re) large-amplitude ($\sim Re$) flaps propagate mainly in the direction orthogonal to the magnetic field curvature[5,12] from the central part of the sheet toward the flanks, with a speed of $\sim 0.1\,V_a$, where V_a is the Alfvén velocity, and quasiperiod of several minutes[5,6,13].

The most fundamental approach to the problem of stability of static hydromagnetic equilibria, based on the energetic principle, is developed in a classical paper of Bernstein, Frieman, Kruskal and Kulsrud[14]. In frame of this method the problem of stability of so-called 2.5-dimensional configurations (i.e., configurations, where plasma and magnetic field parameters do not depend on one of three spacial coordinates) is studied in Ref.[15], and the stability criterion for two-dimensional (2D) magnetotail equilibria with zero dawn-dusk magnetic component is derived by Schindler and Birn in Ref.[16] Particularly, for the antisymmetric modes, i.e. for the kink-like perturbations of the current sheet (CS), the sufficient stability criterion for the ballooning mode, proved to be the most unstable one, is given in their Eq. 54,

$$\left\{ B_x B_z \neq 0, \qquad B_x B_z \frac{\partial^2 B_z}{\partial \Psi \partial z} \leq 0 \right\}, \qquad z > 0, \tag{1}$$

where x and z are the cartesian coordinates, with x-axis pointing tailward, z-axis pointing northward, and y-axis directed dawnward, B_x and B_z are the magnetic field components and Ψ is the magnetic potential. We use this frame and notations throughout the current paper. Criteria (1) assumes that field lines cross the x axis, and the perturbation of the magnetic potential vanishes at the left (ionospheric) boundary.

In application to the subject of our study, we can note that criterion (1) does not supply the practical necessities exactly. First, as the sufficient condition for the ballooning mode stability it may considerably overestimate the necessary and sufficient stability criterion for the flapping mode. Second, the simple form of criterion (1) is appropriate only in the simplest case when the quantity $B_x B_z \partial^2_{\Psi z} B_z$ is of fixed sign within the whole CS. If this quantity changes sign along any field line or it has different signs at different field lines, in such cases

the much more complicated integral quantity is to be calculated (see Eq. (B4) in Ref.[16]). This makes the Schindler-Birn criterion substantially non-local and hardly applicable for satellite data analysis. At last, criterion (1) is undefined at the CS center $z = 0$. At the same time, morphology of the flapping mode allows suggesting that the conditions in the sheet center are dominant for the mode development.

A more appropriate result is derived in the thin CS approximation, developed in the paper[17], where the so-called double-gradient (DG) model of the flapping oscillations was introduced. Stability analysis of the Harris-like CS with additional linear normal magnetic component $B_z(x)$ respective to transversally propagating kink-like perturbations $\sim \exp[i(\omega t - k_y y)]$ yielded the simple dispersion relation[18],

$$\omega = \omega_f \sqrt{\frac{k_y \Delta}{k_y \Delta + 1}}, \tag{2}$$

$$\omega_f^2 = \left(\frac{1}{\mu_0 \rho} \frac{\partial B_x}{\partial z} \frac{\partial B_z}{\partial x} \right)_{z=0}. \tag{3}$$

Here, μ_0 is the permeability of free space, ρ is the plasma mass density, 2Δ is the typical cross-size of the CS, k_y is the wave number and ω is the angular frequency. It is seen that according to the DG model, stability of the CS depends on the sign of the product of two magnetic gradients. Simple analysis shows[19] that the quantity ω_f^2 is positive (sheet is stable) when the total pressure (plasma + magnetic) has a minimum in the sheet center, and ω_f^2 is negative (sheet is unstable) in the opposite case.

It is clear, that this stability criterion, being less general, than criterion (1), is more handy for practical use. At the same time, the numerous simplifying assumptions (incompressibility, sheet scaling) involved in the DG analysis, do not allow accepting the DG model results a priori. Although in some cases the model-based estimates of the typical flapping parameters show a good agreement with those derived from satellite data analysis[17,18,20,21], the practical scope of this model is still in question. Particularly, the DG model implements the stability analysis for the non-equilibrium background magnetic configuration, where the net force is nonzero, while the linear MHD approach implies it to vanish. Besides, the DG model is quasi-one-dimensional, i.e. it does not provide direct predictions for two-dimensional configurations. In paper[22] we performed 2D linear MHD numerical simulations of the flapping mode in the aforementioned magnetic configuration. In the present paper we proceed to the numerical stability analyzes for generalized Fadeev-Manankova[23,24] equilibrium CS and

compare the results with analytical predictions of the DG model.

The paper is organized as follows. Section II describes the CS model and numerical simulations setup. Results of the numerical simulations are compared with analytical predictions in Section III. Section IV embraces summary and discussion.

II. SETUP

In this section we specify the background magnetoplasma configuration and outline our methodology in brief, the more detailed description is provided in Ref.[22]

The generalized Harris-Fadeev-Kan-Manankova model of the background equilibria is given by the following expressions[25],

$$\Psi = \ln\left[\frac{f\cos(X_*) + \sqrt{1+f^2}\cosh(Z_*)}{\sqrt{W}}\right], \tag{4}$$

$$X_* = x - \frac{b\cos(k\theta)}{R^k}, \tag{5}$$

$$Z_* = z + \frac{b\sin(k\theta)}{R^k}, \tag{6}$$

$$W = \left(1 + \frac{kb}{R^{k+1}}\right)^2 - \frac{4kb}{R^{k+1}}\sin^2\left(\frac{(k+1)\theta}{2}\right), \tag{7}$$

$$R = \sqrt{(x-a)^2 + z^2}, \tag{8}$$

$$\theta = \arctan\left(\frac{z}{x-a}\right). \tag{9}$$

Here, $\{a,\, b,\, f,\, k\}$ are the model parameters and Ψ is the magnetic potential. The physical quantities are expressed via Ψ and its derivatives,

$$B_x = -\frac{\partial\Psi}{\partial z}, \qquad B_z = +\frac{\partial\Psi}{\partial x}, \tag{10}$$

$$\rho = \exp\left(-2\Psi\right) + \rho_b, \tag{11}$$

$$p = 0.5\exp\left(-2\Psi\right), \tag{12}$$

where p is the plasma pressure, and ρ_b is a small constant term representing the contribution of the additional cold plasma population (required to reduce the Alfvén velocity in numerical simulations). The third component of the background magnetic field, B_y, is identically zero, as well as the plasma velocity $\mathbf{V}$.

The set of compressional ideal MHD equations[26] is solved numerically using the perturbation technique. All variables are represented as a sum of two terms: the equilibrium state U_0,

and a small perturbation U_1, hence MHD equations are linearized. The solution U_1 is found in the form of a wave, propagating across the CS in y direction: $U_1 = \delta U \exp(ik_y y)$, where the perturbation amplitude is $\delta U(x, z, t; k_y)$. Therefore, the system of linearized equations for amplitudes takes the conservative form,

$$\frac{\partial(\delta \mathbf{U})}{\partial t} + \frac{\partial \mathbf{F}_x}{\partial x} + \frac{\partial \mathbf{F}_z}{\partial z} = \mathbf{S}, \tag{13}$$

where

$$\delta \mathbf{U} = (\delta\rho, \{\delta M_i\}, \{\delta B_i\}, \delta E)_{i=x,y,z}\,. \tag{14}$$

The variable $\mathbf{U}$ denotes the vector of normalized plasma parameters, where $M_i = \rho V_i$ is the momentum, $E = p/(\kappa - 1) + 0.5\rho V^2 + 0.5B^2$ is the total energy density, and κ is the polytropic index (the value of 5/3 is utilized). The set of normalization constants includes the sheet half-width Δ, the lobe magnetic field B_0, $p_0 = B_0^2/\mu_0$ for pressure, the peaking value of the mass density in the sheet center, ρ_0, the Alfvén velocity $V_a = B_0/\sqrt{\mu_0\rho_0}$, and time $t_0 = \Delta/V_a$. The expressions for the flux densities $\mathbf{F}_x$ and $\mathbf{F}_z$ and for the source function $\mathbf{S}$ are given in Appendix A of Ref.[22] In this way, the initial system of equations is reduced to a time-dependent two-dimensional problem for complex quantities $\delta\mathbf{U}$, while physically meaningful functions are $\Re[\delta\mathbf{U}\exp(ik_y y)]$. Simulations are seeded with initial perturbation $\delta V_z|_{t=0} = \exp(-z^2)$. Under these conditions the vector of unknowns consists of eight non-zero terms: $\Re(\delta\rho)$, $\Re(\delta M_x)$, $\Im(\delta M_y)$, $\Re(\delta M_z)$, $\Re(\delta B_x)$, $\Im(\delta B_y)$, $\Re(\delta B_z)$, $\Re(\delta E)$. In the following, we omit the subscript $< 0 >$ in the notations of background quantities.

Equations (13) are solved numerically by means of the 3rd order central semi-discrete upwind scheme[27] with open boundary conditions $\partial \cdot /\partial \mathbf{n} = 0$. We have used the optimal (in the sense of Courant-Friedrichs-Lewy (CFL) coefficient and the computational cost) strong stability preserving Runge-Kutta method of the 3rd order described in Ref.[28] The integration time step (CFL number = 0.5) is adopted to ensure the convergence of the results with respect to values of the time step. The $(\nabla \cdot \mathbf{B}) = 0$ constraint is enforced on each time step by using the method of projection[29].

The results of 2D numerical simulations are compared to the quasi-1D DG model, representing the solution of Eq. (13) under the following simplifying scaling assumptions[17]: a) the CS is stretched, so that $\nu = \Delta/L_x \ll 1$, where L_x is the typical sheet length; b) the normal magnetic component is small, so that $\epsilon = \max(B_z)/\max(B_x) \ll 1$; and c) $\epsilon/\nu \ll 1$. Under these assumptions the terms of the order of $\nu^2\epsilon$ and ϵ^2 are neglected (see underlined

terms of Eq. (10) in Ref.[18]) and system (13) is reduced to a single equation for perturbation of the normal velocity component, v_z,

$$\frac{1}{\rho}\frac{d}{dz}\left(\rho\frac{dv_z}{dz}\right) + k_y^2 v_z\left(\frac{U_0}{\omega^2} - 1\right) = 0, \tag{15}$$

where the function

$$U_0 = \frac{1}{\rho}\frac{\partial B_x}{\partial z}\frac{\partial B_z}{\partial x} \tag{16}$$

and all other quantities are assumed to be independent of the x coordinate. The spectral problem is set by completing Eq. (15) with boundary conditions

$$v_z(0) = 1, \quad \frac{dv_z}{dz}(0) = 0, \tag{17}$$

$$\frac{dv_z}{dz}(z_b) = -k_y v_z(z_b). \tag{18}$$

Here, conditions (17) specify the kink-like perturbation of the CS, z_b is the upper z-boundary, proxy of the infinity, and condition (18) assumes v_z to decrease exponentially outside the CS. For $B_x \sim \tanh(z)$, $B_z \sim x$ and uniform background mass density the analytical solution (2–3) of the spectral problem (15–18) is derived in Ref.[18]; it represents the dispersion relation for the fastest growing/oscillating mode.

III. RESULTS

Setting background model parameters to $a = 0$, $b = 1$, $f = 0.1$, $k = 10$ and $\rho_b = 0.1$, we derive the Fadeev-like magnetic configuration (see Fig. 1 in Ref.[25]). We consider the domain $x \in [x_0 - 3,\, x_0 + 3]$, symmetrical with respect to the X-line location $x_0 \approx 12.6$. The box is symmetrical also with respect to the CS center $z = 0$. The location of z-boundaries varies depending on k_y because eigenfunctions broaden with decreasing wave number (see Fig. 5 in Ref. [22]). Fig. 1a shows the magnetic potential Ψ and field lines, in Fig. 1b the total pressure Π is plotted. We see that in the central part of the domain the total pressure reaches a minimum at the x axis (stable region), while at the flanks Π demonstrates maximum at $z = 0$ (unstable regions). In Fig. 1c the normalized quantity U_0 by Eq. (16) is depicted; the sign of U_0 changes synchronously with the total pressure behavior. Note the DG typical frequency $\omega_f = \sqrt{U_0(z=0)}$. Fig. 1d plots the Schindler-Birn stability criterion, calculated from the Eq. (1). It is seen that the quantity $B_x B_z \partial^2_{\Psi_z} B_z$ is not of constant sign. Criterion

(1) predicts stability only for the computational boxes bounded within the region, where Π exhibits minimum in the sheet center; for wider boxes it is not appropriate.

Fig. 2 shows the dispersion relation $\gamma(k_y)$, where $\gamma = \Im(\omega)$. Calculations are performed with three values of the uniform grid step: $dx = dz = 1/2^4$ (blue asterisks), $1/2^5$ (green curve), and $1/2^6$ (red crosses). It is seen that the numerical scheme demonstrates a fast grid convergency, so that for not too large values of k_y the grid step $1/2^5$ is quite appropriate. For smaller values $k_y \sim 1$ or less, the grid step may be increased even more – up to $1/2^4$. Then we see that for any k_y the sheet average growth rate coincides with the single-point quantity, i.e. instability develops uniformly. For reference, the DG analytical dispersion relation (2) is shown by a black curve (the solution for Harris-like CS with a constant mass density), where the maximum over the sheet value of $\gamma_f = \Im(\omega_f)$ is used. Red dashed curve plots the solution of the one-dimensional spectral problem (15–18) in the cross-section $x = x_0 - 2.5$. It is seen that green and red curves show rather good agreement in the low-wavelength range $k_y > 4$, the maximum discrepancy $\sim 10\%$ is reached at $k_y \approx 1$. The simplest analytical estimate (black curve) overtops the numerical solution for 10% approximately uniformly in the wavenumber range $k_y > 2$.

On Fig. 3 numerical solutions for perturbations $v_z(x_0, z)$ for $k_y = \{1, 2, 3\}$ are compared with the solutions of problem (15–18). It is seen that for small values of wave number analytical and numerical solutions demonstrate rather good match, which fades with increasing k_y.

Fig. 4 shows the quantity $\omega^2(k_y = k_y^{max})$, computed in symmetric computational box $x \in [x_0 - \Delta x, x_0 + \Delta x]$, as a function of the right boundary location (green crosses). The maximum value of wave number $k_y^{max} = 10$ for instability and 20 for oscillations. Reducing the box size in the x direction, we reduce the unstable part of the CS, where the total pressure has a maximum in the sheet center (see Fig. 1b). It is seen that the growth rate absolute value decreases with the unstable region trimming. The red solid curve shows the quantity $U_0(z = 0)$, calculated from the formula (16), and the red dashed curve shows the average negative value of $U_0(z = 0)$. Notably, the entire sheet turns out to be unstable independently on the size of the intrinsically unstable region. However, the quantity γ^2 fits the average negative value of U_0, hence an infinitely small unstable spot would destabilize a sheet for an infinitely long time. The values of $\omega^2(k_y^{max})$ from the solution of the spectral problem (15–18) in the corresponding cross-sections are shown by black circles. Expectably,

these values match the quantity $U_0(z=0)$ with an accuracy of several percents.

When the simulation box does not contain any unstable spot, the sheet demonstrates a stable behavior with almost harmonic oscillations, except of slow numerical attenuation with the exponent factor $\sim 10^{-2} - 10^{-3}$, depending on wave number, as it is shown in Fig. 5. Normalized Fourier spectra for averaged perturbations (averaging on the third quadrant $[x < x_0, z < 0]$) for $k_y = 1$ are shown in Fig. 6. This plot demonstrates that the low-frequency oscillations are excited at the maximum DG frequency. The dispersion curve of these oscillations, shown in Fig. 7, does approach the DG prediction in short- and long-wavelength segments. The major difference is manifested in a local hump of $\omega(k_y)$ at $k_y \approx 8.7$, i.e. at wavelength $\lambda \approx 0.7\Delta$. Accuracy of the obtained dispersion relation $\omega(k_y)$ is limited by the frequency step $d\omega = 2\pi/t_{max}$, in our case this value is 0.0063. The difference between single-point and sheet-averaged frequencies does not exceed $d\omega$ (except of the hump peak); the finite value of $d\omega$ is also the reason of flat segments at blue and red curves. The limiting low-wavelength frequency is very close to the DG maximum estimate and does not depend on the box width, as it is seen in Fig. 4.

The high-frequency eigenmodes, observed on Fig. 6, propagate with group velocities of 1 (close to the maximum background sound speed, 0.85) and 3 (close to maximum background Alfvén velocity, 3.1), respectively. Contrary to the flapping mode, these eigenmodes, produced by initial perturbation $V_z = \exp(-z^2)$, are preserved in the Harris CS, where the only oscillating quantities, δV_y and δV_z, produce the vortex motion. The very low-frequency peaks of Fourier spectra of δM_x, δB_y and δB_z, viewed on Fig. 6 to the left of DG mode, are non-physical noises.

IV. SUMMARY AND DISCUSSION

In this paper we present a case study of the MHD stability of the Fadeev-like CS with respect to transversally propagating kink-like perturbations (flapping mode). Results of 2D numerical simulations agree with analytical predictions of the quasi-one-dimensional DG model. We used symmetric simulation boxes centered at the X-line in the x direction and at $z = 0$ in the z direction. Central part of the investigated domain, where total pressure Π attains minimal values at $z = 0$, is appeared to be stable, while flanks, where Π peaks at the x axis, are found to be unstable.

It is shown that unstable part of any size, seized by simulation box, drives the whole sheet to unstable regime. In such case increment of instability γ decreases with the reduction of unstable domain, so that the value of γ^2 fits the average negative ω_f^2 by Eq. (3) of the DG model. One-dimensional analytical model supports this result: best match of analytical and numerical dispersion curves and eigenfunctions are obtained in some approximately central cross-section of the unstable region. Even the simplest analytical solution $(2, 3)$ yields the reasonable 10% accurate estimate of the dispersion relation. From the perspective of satellite data analysis, the 2D and 1D solutions are virtually indistinguishable, except for a very long-wavelength range $k_y \sim 0.1/\Delta$.

When the entire simulation box is located within the stable part of the sheet, the typical frequency of oscillations (short-wavelength limit) demonstrates a high-accurate match with the maximum DG estimate. The numerically obtained dispersion curve is steeper than the DG predicted one in long-wavelength range, and overtops it slightly everywhere. The first effect is produced by the non-uniformity of the mass density[18], while formula (2) was derived under the condition $\rho = const$. The second effect is related to the approximate nature of the estimate of ω_f^2 as $\langle U_0 \rangle |_{U_0<0}$ (see Fig. 4). The local maximum on the dispersion curve at the wavelength $\lambda \sim 0.7\Delta$ is a new feature, which has not been captured by the DG model. It represents the contribution of all terms of linear MHD system, that have been neglected in analytical solution (see Eq. 10 in Ref.[18]). As for the rest, the good match of numerical and analytical solutions is supported by the appropriate scaling of the examined background configuration, where $\nu = \Delta/L_x \sim 0.5$ and $\epsilon = \max(B_z)/\max(B_x) = 0.1$.

Thus, results of 2D numerical simulations with an equilibrium background configuration demonstrate two important features, missed in previous studies with non-equilibrium background. In a stable CS, this is a local maximum of the dispersion curve, which was not observed in simulations[22] with Harris-like CS with the X-point – at first sight, rather similar to the current model. The second feature is revealed in simulations of unstable CS, where the typical growth rate matches the sheet-averaged DG estimate, while in non-equilibrium configuration it was scaled as the sheet maximum value. For details, see Ref.[30], where the sheet-averaged estimate was found matching the results of nonlinear 3D MHD simulations only (notable, in 3D simulations the background configuration was numerically relaxed to equilibrium state).

It may seem that the condition of CS stability with respect to the flapping mode may be

expressed in two equivalent ways: maximum/mimimum of the total pressure in the sheet center, and sign of the quantity $U_0(z=0)$. This is not exactly true. The behavior of the total pressure, not U_0, is the key factor controlling the stability. Indeed, due to symmetry Π may demonstrate only a minimum or maximum in the sheet center. Assuming that the quantity $\partial\Pi/\partial z$ is continuous, we conclude that a minimum of the total pressure means the positiveness of its second derivative on z in the sheet center. In static equilibrium, where $\nabla\Pi = (\mathbf{B}\cdot\nabla)\mathbf{B}$, we have

$$\frac{\partial^2\Pi}{\partial z^2} = \frac{\partial B_x}{\partial z}\frac{\partial B_z}{\partial x} + B_z\frac{\partial^2 B_z}{\partial z^2} + B_x\frac{\partial^2 B_z}{\partial x \partial z} + \left(\frac{\partial B_z}{\partial z}\right)^2. \tag{19}$$

At the x axis the last two terms on the right-handed side of Eq. (19) vanish due to the symmetry. The first term represents the function U_0 of the DG model multiplied by ρ. The second term may be neglected in thin current sheets but not in the general case. When this term is neglected, the condition $\partial^2\Pi/\partial z^2 > 0$ is identical to the condition $U_0(x,0) > 0$, yielding in turn $\partial B_z/\partial x < 0$ (in an adopted reference system, where $\partial B_x/\partial z < 0$), i.e. the sheet is stable when B_z is growing earthward, which is a well-known marker (see, e.g., Refs.[31,32]). However, in the general case the second term on the right-handed side of Eq. (19) may result in some difference between predictions based on the behavior of the total pressure and the function U_0.

It is easy to assure that the stability criterion, expressed via a condition of the central minimum of total pressure, has a clear physical sense. Using the divergence-free condition, we can rewrite Eq. (19) at the x axis as follows,

$$\frac{\partial^2\Pi}{\partial z^2}(x,0) = \frac{\partial B_x}{\partial z}\frac{\partial B_z}{\partial x} - B_z\frac{\partial^2 B_x}{\partial x \partial z} = -B_z^2\frac{\partial}{\partial x}\left(\frac{1}{B_z}\frac{\partial B_x}{\partial z}\right), \tag{20}$$

where the under-derivative term on the right-handed side is nothing but κ_c, the curvature of the magnetic field line at the x axis. Hence, the stability condition $\partial^2\Pi(x,0)/\partial z^2 > 0$ takes the form

$$\left(\frac{\partial \kappa_c}{\partial x}\right)_{z=0} < 0. \tag{21}$$

The sign of curvature depends on the reference system and magnetic configuration. In the coordinate system adopted in this paper, curvature is negative to the left of the X-line and positive to the right. Thus, the stability criterion claims that the CS is stable with respect to the MHD flapping mode, if the magnetic field curvature radius, $R_c = 1/|\kappa_c(x,0)|$, is

decreasing in the tailward direction before the X-line (sheet is thinning), and R_c is increasing behind the X-line (sheet is thickening).

The direct comparison of criterion (21) and Schindler-Birn criterion (1) and its general form (B4) in Ref.[16] is problematic, if only because these two expressions have different regions of definition. At any rate, numerical simulations in the pure stable domain reveal that these two criteria do not contradict each other. However, in point of the flapping mode criterion (21) has some substantial advantages. First, it provides the necessary and sufficient condition for the mode stability. Second, it is "more local", because it requires calculations along the sheet center only, not within the entire domain.

In stretched current sheets the quantity $\partial^2\Pi/\partial z^2$ may take rather small values. However, reduction of $\partial^2\Pi/\partial z^2$ does not reduce the effectiveness of this quantity, it only reduces the typical frequency/growth rate of the flapping mode. It demonstrates the limitation of the boundary layer approximation: the last one implies that in sufficiently stretched current sheets the total pressure across the sheet may be assumed constant. Under this assumption the flapping mode is totally lost. It is also notable that criterion (21) is derived for the exact equilibria, where $\nabla p = \mathbf{j} \times \mathbf{B}$. If the force balance is corrupted, as it takes place in approximate equilibria solutions, criterion (21) may be inappropriate. Particularly, the approximate solution in the form $\Psi = \ln\{\cosh[F(\epsilon x)z]/F(\epsilon x)\} + O(\epsilon^2)$, introduced in Ref.[33], may appear to be not sufficiently accurate. Here, the small parameter ϵ characterizes the ratio of the system typical sizes in z and x directions. If the quantity $B_z(x,0)/B_x(x,z_b)$ is also of the order of ϵ, in such a case Eq. (20) yields that at the x axis $\partial^2\Pi/\partial z^2 \sim \epsilon^2$.

As previously noted, the condition (21) is mostly controlled by the sign of the derivative $\partial B_z/\partial x$. According to Cluster statistics[34], in the Earth magnetotail behind $14\,Re$ at the substorm growth phase the growth direction of B_z is fluctuating with time scales of $5-15$ min. Our simulations reveal that kink-like deformations of the magnetotail CS should start to grow, probably slowly, any time, when B_z is increasing tailward. Then, when the sign of $\partial B_z/\partial x$ changes, this deformation plays a role of initial perturbation for the flapping wave, propagating toward the flanks. Analytically, such mechanism was studied in Ref.[35]

At first sight, it may seem that according to our findings the magnetotail should never be quiet, which is not true. Indeed, the non-local destabilization of the CS means that the near-tail high-density plasma should impede the instability considerably. Other effective stabilizing factors are the interaction with ionosphere[36], non-zero magnetic component B_y[37]

and, possibly, shear flows[38,39].

As it was stated above, in the present case the CS scaling matches the assumptions of the analytical DG model, hence a good agreement of analytical and numerical results is observed. In the general case this agreement of scalings may be corrupted and cross-checking of 1D and 2D solutions may become not possible any more. Then, results of 2D simulations may be verified by means of fully 3D modeling only. Unfortunately, in 3D there are no simple analytical solutions for background magnetoplasma equilibrium, therefore the problem turns much more complicated. One of the possible approaches utilizes a quasi-3D model, when the 2D configuration is replicated in the third direction (see, e.g., Refs.[40,41]). Though not exact, this approach serves as a reasonable proxy for quasi-2D processes studies. Particularly, it was successfully applied for simulations of the lower hybrid drift instability at reconnection jet fronts[42], energy conversion at dipolarization fronts[43], and DG instability.[30]

ACKNOWLEDGMENTS

The work of D. B. K. and S. A. K. was supported by the Austrian Science Fund (FWF): P 27012-N27. V. S. S was supported by RFBR grant No 16-05-00470-a, and the work of N. V. E. and I. I. R. was supported by RFBR grants No 15-05-00879-a and 18-05-00195_a. Authors thank the reviewer for his help in the manuscript improvement.

REFERENCES

[1]N. F. Ness, "The Earth's magnetic tail," J. Geophys. Res. **70**, 2989–3005 (1965).

[2]V. Sergeev, V. Angelopoulos, C. Carlson, and P. Sutcliffe, "Current sheet measurements within a flapping plasma sheet," J. Geophys. Res. **103**, 9177–9187 (1998).

[3]T. L. Zhang, W. Baumjohann, R. Nakamura, A. Balogh, and K. H. Glassmeier, "A wavy twisted neutral sheet observed by Cluster," Geophys. Res. Lett. **29**, 1899 (2002).

[4]C. Shen, X. Li, M. Dunlop, Z. X. Liu, A. Balogh, D. N. Baker, M. Hapgood, and X. Wang, "Analyses on the geometrical structure of magnetic field in the current sheet based on cluster measurements," J. Geophys. Res. **108**, 1168 (2003).

[5]A. Runov, V. A. Sergeev, W. Baumjohann, R. Nakamura, S. Apatenkov, Y. Asano, M. Vol-

werk, Z. Vörös, T. L. Zhang, A. Petrukovich, *et al.*, "Electric current and magnetic field geometry in flapping magnetotail current sheets," Ann. Geophys. **23**, 1391–1403 (2005).

[6]A. A. Petrukovich, W. Baumjohann, R. Nakamura, A. Runov, A. Balogh, and C. Carr, "Oscillatory magnetic flux tube slippage in the plasma sheet," Ann. Geophys. **24**, 1695–1704 (2006).

[7]Z. Rong, C. Shen, A. Petrukovich, W. Wan, and Z. Liu, "The analytic properties of the flapping current sheets in the earth magnetotail," Planet. Space Sci. **58**, 1215–1229 (2010).

[8]G. Wang, M. Volwerk, R. Nakamura, P. Boakes, T. Zhang, A. Yoshikawa, and D. Baishev, "Flapping current sheet with superposed waves seen in space and on the ground," J. Geophys. Res.: Space Phys. **119**, 10078 (2014).

[9]Z. Rong, S. Barabash, G. Stenberg, Y. Futaana, T. Zhang, W. Wan, Y. Wei, X. Wang, L. Chai, and J. Zhong, "The flapping motion of the Venusian magnetotail: Venus Express observations," J. Geophys. Res.: Space Phys. **120**, 5593–5602 (2015).

[10]B. H. Mauk, D. C. Hamilton, T. W. Hill, G. B. Hospodarsky, R. E. Johnson, C. Paranicas, E. Roussos, C. T. Russell, D. E. Shemansky, E. C. Sittler, *et al.*, "Fundamental plasma processes in Saturn's magnetosphere," in *Saturn from Cassini-Huygens*, edited by M. K. Dougherty, L. W. Esposito, and S. M. Krimigis (Springer, 2009) pp. 281–331.

[11]M. Volwerk, N. André, C. S. Arridge, C. M. Jackman, X. Jia, S. E. Milan, A. Radioti, M. F. Vogt, A. P. Walsh, R. Nakamura, *et al.*, "Comparative magnetotail flapping: an overview of selected events at Earth, Jupiter and Saturn," Ann. Geophys. **31**, 817–833 (2013).

[12]A. Runov, V. Angelopoulos, V. A. Sergeev, K. H. Glassmeier, U. Auster, J. McFadden, D. Larson, and I. Mann, "Global properties of magnetotail current sheet flapping: THEMIS perspectives," Ann. Geophys. **27**, 319–328 (2009).

[13]V. Sergeev, A. Runov, W. Baumjohann, R. Nakamura, T. L. Zhang, M. Volwerk, A. Balogh, H. Rème, J. A. Sauvaud, M. André, and B. Klecker, "Current sheet flapping motion and structure observed by cluster," Geophys. Res. Lett. **30**, 1327 (2003).

[14]I. B. Bernstein, E. A. Frieman, M. D. Kruskal, and R. M. Kulsrud, "An Energy Principle for Hydromagnetic Stability Problems," Proc. Royal Society of London A: Mathematical, Physical and Engineering Sciences **244**, 17–40 (1958).

[15]K. Schindler, J. Birn, and L. Janicke, "Stability of two-dimensional pre-flare structures," Solar Phys. **87**, 103–133 (1983).

[16]K. Schindler and J. Birn, "MHD stability of magnetotail equilibria including a background pressure," J. Geophys. Res. **109**, 10208 (2004).

[17]N. V. Erkaev, V. S. Semenov, and H. K. Biernat, "Magnetic double-gradient instability and flapping waves in a current sheet," Phys. Rev. Lett. **99**, 235003 (2007).

[18]N. V. Erkaev, V. S. Semenov, I. V. Kubyshkin, M. V. Kubyshkina, and H. K. Biernat, "MHD aspect of current sheet oscillations related to magnetic field gradients," Ann. Geophys. **27**, 417–425 (2009).

[19]N. V. Erkaev, V. S. Semenov, I. V. Kubyshkin, M. V. Kubyshkina, and H. K. Biernat, "MHD model of the flapping motions in the magnetotail current sheet," J. Geophys. Res. **114**, A03206 (2009).

[20]C. Forsyth, M. Lester, R. C. Fear, E. Lucek, I. Dandouras, A. N. Fazakerley, H. Singer, and T. K. Yeoman, "Solar wind and substorm excitation of the wavy current sheet," Ann. Geophys. **27**, 2457–2474 (2009).

[21]W. Sun, S. Fu, Q. Shi, Q. Zong, Z. Yao, T. Xiao, and G. Parks, "THEMIS observation of a magnetotail current sheet flapping wave," Chin. Sci. Bull. **59**, 154–161 (2014).

[22]D. Korovinskiy, I. Ivanov, V. Semenov, N. Erkaev, and S. Kiehas, "Numerical linearized MHD model of flapping oscillations," Phys. Plasmas **23**, 062905 (2016).

[23]V. Fadeev, I. Kvartskhava, and N. Komarov, "Self-focusing of the local plasma current sheets (in Russian)," Nucl. Fusion **5**, 202–209 (1965).

[24]A. Manankova, M. Pudovkin, and A. Runov, "Stationary configurations of the two-dimensional current-carrying plasma sheet: Exact solutions," Geomagnetism and Aeronomy c/c of Geomagnetizm i Aeronomiia **40**, 430–438 (2000).

[25]P. H. Yoon and A. T. Y. Lui, "A class of exact two-dimensional kinetic current sheet equilibria," J. Geophys. Res. **110**, A01202 (2005).

[26]A. G. Kulikovskii, N. V. Pogorelov, and A. Y. Semenov, *Mathematical aspects of numerical solution of hyperbolic systems* (CRC Press, 2000).

[27]A. Kurganov, S. Noelle, and G. Petrova, "Semidiscrete central-upwind schemes for hyperbolic conservation laws and Hamilton–Jacobi equations," SIAM J. Sci. Comp. **23**, 707–740 (2001).

[28]S. Gottlieb, C.-W. Shu, and E. Tadmor, "Strong stability-preserving high-order time discretization methods," SIAM Rev. **43**, 89–112 (2001).

[29]G. Tóth, "The $\nabla \cdot B = 0$ Constraint in Shock-Capturing Magnetohydrodynamics Codes,"

J. Comp. Phys. **161**, 605–652 (2000).

[30]D. B. Korovinskiy, A. Divin, N. V. Erkaev, V. V. Ivanova, I. B. Ivanov, V. S. Semenov, G. Lapenta, S. Markidis, H. K. Biernat, and M. Zellinger, "MHD modeling of the double-gradient (kink) magnetic instability," J. Geophys. Res. **118**, 1146–1158 (2013).

[31]L. N. Hau, R. A. Wolf, G. H. Voigt, and C. C. Wu, "Steady state magnetic field configurations for the Earth's magnetotail," J. Geophys. Res. **94**, 1303–1316 (1989).

[32]P. L. Pritchett and F. V. Coroniti, "A kinetic ballooning/interchange instability in the magnetotail," J. Geophys. Res. **115**, A06301 (2010).

[33]K. Schindler, "A self-consistent theory of the tail of the magnetosphere," in *Earth's magnetospheric processes*, Vol. 32, edited by B. M. McCormac (D. Reidel, Dordrecht, Holland, 1972) pp. 200–209.

[34]A. A. Petrukovich, A. V. Artemyev, R. Nakamura, E. V. Panov, and W. Baumjohann, "Cluster observations of $\partial Bz/\partial x$ during growth phase magnetotail stretching intervals," J. Geophys. Res. **118**, 5720–5730 (2013).

[35]D. I. Kubyshkina, D. A. Sormakov, V. A. Sergeev, V. S. Semenov, N. V. Erkaev, I. V. Kubyshkin, N. Y. Ganushkina, and S. V. Dubyagin, "How to distinguish between kink and sausage modes in flapping oscillations?" J. Geophys. Res. **119**, 3002–3015 (2014).

[36]N. Erkaev, V. Semenov, and H. Biernat, "Current sheet oscillations in the magnetic filament approach," Phys. Plasmas **19**, 062905 (2012).

[37]D. Korovinskiy, A. Divin, N. Erkaev, V. Semenov, A. Artemyev, V. Ivanova, I. Ivanov, G. Lapenta, S. Markidis, and H. Biernat, "The double-gradient magnetic instability: Stabilizing effect of the guide field," Phys. Plasmas **22**, 2904 (2015).

[38]A. F. Viñas and T. R. Madden, "Shear flow-ballooning instability as a possible mechanism for hydromagnetic fluctuations," J. Geophys. Res. **91**, 1519–1528 (1986).

[39]T. Tajima, W. Horton, P. J. Morrison, J. Schutkeker, T. Kamimura, K. Mima, and Y. Abe, "Instabilities and vortex dynamics in shear flow of magnetized plasmas," Phys. Fluids **3**, 938–954 (1991).

[40]M. V. Goldman, D. L. Newman, and P. Pritchett, "Vlasov simulations of electron holes driven by particle distributions from PIC reconnection simulations with a guide field," Geophys. Res. Lett. **35**, L22109 (2008).

[41]A. Divin, G. Lapenta, S. Markidis, D. L. Newman, and M. V. Goldman, "Numerical simulations of separatrix instabilities in collisionless magnetic reconnection," Phys. Plasmas

454 **19**, 042110 (2012).
455 [42]A. Divin, Y. V. Khotyaintsev, A. Vaivads, M. André, S. Markidis, and G. Lapenta,
456 "Evolution of the lower hybrid drift instability at reconnection jet front," J. Geophys.
457 Res.: Space Phys. **120**, 2675–2690 (2015).
458 [43]Y. V. Khotyaintsev, A. Divin, A. Vaivads, M. André, and S. Markidis, "Energy conversion
459 at dipolarization fronts," Geophys. Res. Lett. **44**, 1234–1242 (2017).

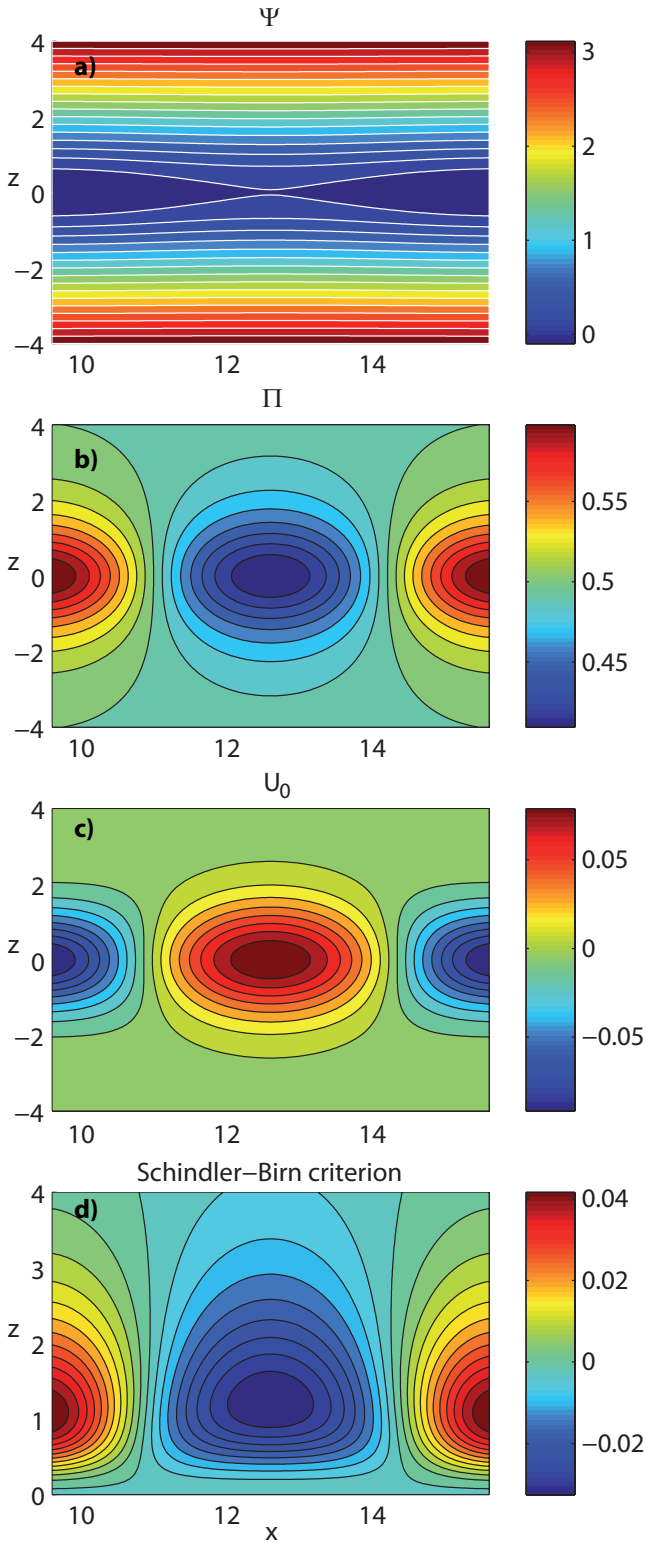

FIG. 1. Background magnetic configuration: a) magnetic potential (color) and field lines (white); b) total pressure; c) the function U_0 (16); d) Schindler-Birn stability criterion (1).

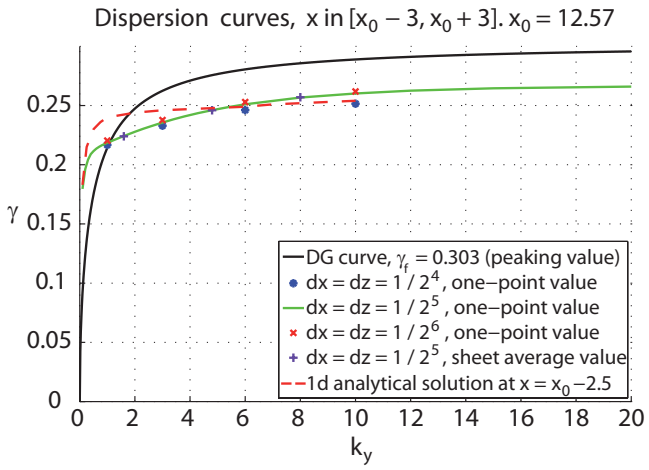

FIG. 2. Results of simulations in the symmetric interval $x \in [x_0 - 3, x_0 + 3]$, where x_0 is the X-line location. The numerically derived dispersion relation of instability, calculated in a single point, located in the sheet center $[x_0 - dx/2, -dz/2]$, is shown by the green curve for the grid step $dx = dz = 1/2^5$, analogous dispersion relation, computed with the grid step $1/2^4$ is shown by blue asterisks, and red crosses represent the results for $dx = dz = 1/2^6$. Sheet-averaged growth rate ($dx = dz = 1/2^5$) is depicted by violet crosses. The black curve shows analytical dispersion relation (2), where for ω_f^2 the sheet minimum value is utilized. The red dashed curve shows the analytical solution of the one-dimensional problem (15–18) at the cross-section $x = x_0 - 2.5$.

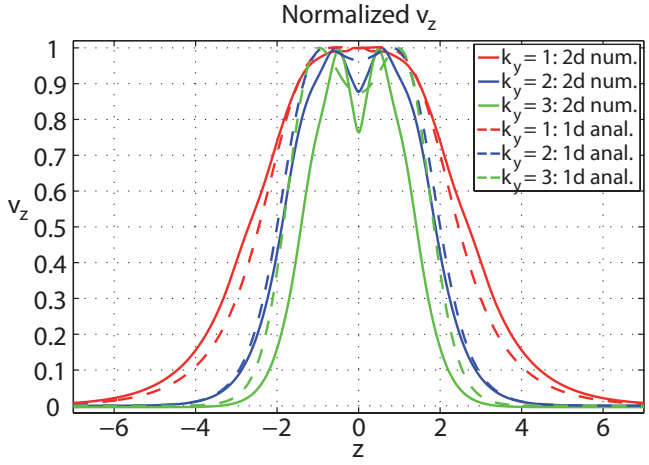

FIG. 3. Normalized numerical solutions for the velocity perturbation v_z are shown by solid curves for $k_y = \{1, 2, 3\}$ by red, blue and green curves, respectively. Analytical eigenfunctions $v_z(z, x = x_0 - 2.5)$ for the same values of k_y, calculated from Eq. (15–18), are shown by dashed curves of the same colors.

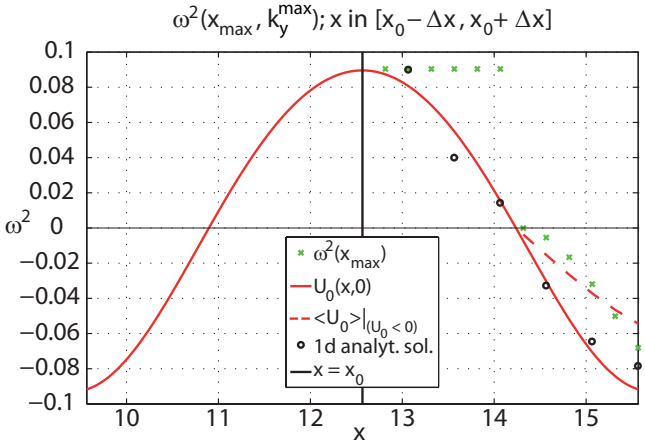

FIG. 4. The quantity $\omega^2(k_y^{max})$ is shown by green crosses as a function of the right boundary of the symmetric computational box $x \in [x_0 - \Delta x, x_0 + \Delta x]$. The red solid curve shows the quantity $U_0(z = 0)$ from Eq. (16), and the red dashed curve plots average negative values of $U_0(z = 0)$. Black circles show $\omega^2(k_y^{max})$ from the solution of one-dimensional spectral problem (15–18). The maximum value of the wave number $k_y^{max} = 10$ for unstable mode, and 20 for stable regime.

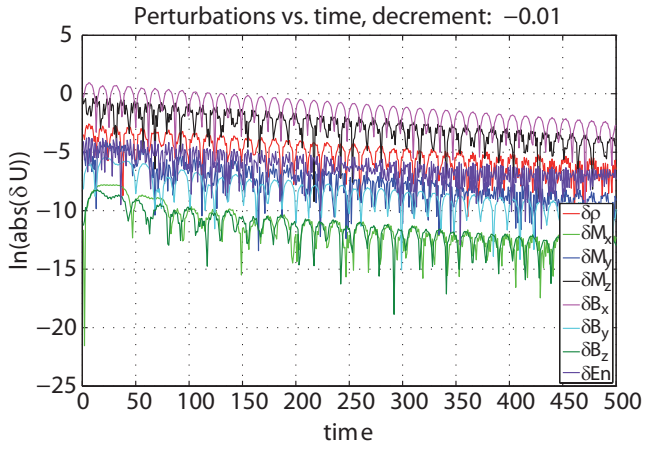

FIG. 5. Time evolution of logarithms of the perturbation absolute values, calculated in the point $[x_0 - dx/2, -dz/2]$ for $k_y = 1$. Color scheme: $\delta\rho$ (red), δM_x (light-green), δM_y (blue), δM_z (black), δB_x (magenta), δB_y (cyan), δB_z (dark-green), and perturbation of energy δEn (violet).

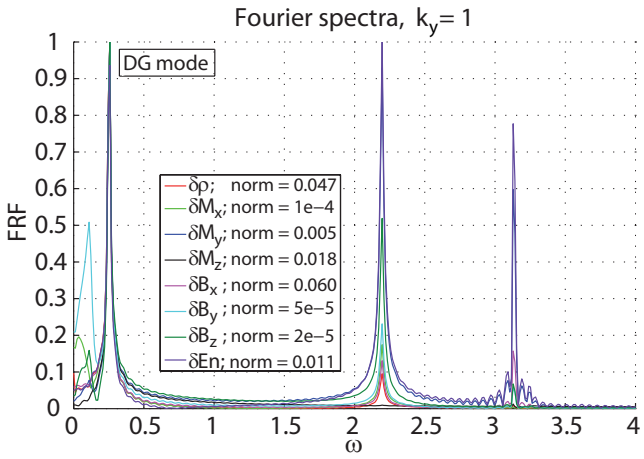

FIG. 6. Normalized Fourier spectra of oscillations averaged over the third quadrant $[x < x_0,\, z < 0]$ for $k_y = 1$. Color scheme is the same as in Fig. 5. Normalization factors are given in the figure legend.

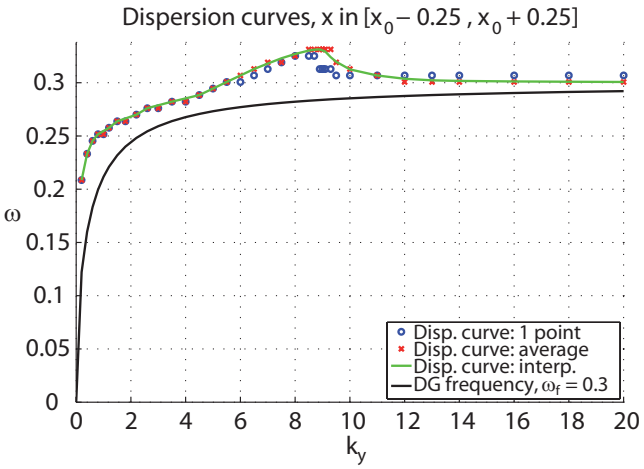

FIG. 7. Dispersion relation of oscillations in the stable region $x \in [x_0 - 0.25,\, x_0 + 0.25]$. Blue circles show single-point values in the sheet center, red crosses show sheet-averaged values (averaging on the 3rd quadrant), green curve interpolates the red one, and black curve plots DG analytical prediction (2) with $\omega_f = \sqrt{\max(U_0)}$.